RSC Advances

ROYAL SOCIETY OF CHEMISTRY

www.rsc.org/advances

Indium-tin-oxide nanorods for efficient light trapping in polymer solar cells†

Yu-Chiang Chao,[*ab] Fu-Min Zhan,[a] and Husan-De Li,[a]

[a] Department of Physics, Chung Yuan Christian University, Chung-Li 32023, Taiwan

[b] Center for Nanotechnology, Chung Yuan Christian University, Chung-Li 32023, Taiwan

*E-mailycchao@cycu.edu.tw

† Electronic supplementary information (ESI) available.

KEYWORDS: Polymer solar cells, photovoltaics, light trapping, light scattering

ABSTRACT:

In this study, a wet chemical method of etching indium-tin-oxide (ITO) nanorods from commercially available ITO-coated glass is proposed and its applicability in polymer solar cells (PSCs) is validated. The ITO nanorods can be fabricated within a few minutes using the proposed method. The ITO-nanorods-based PSCs show 67% and 46% improvement in short-circuit current density and power conversion efficiency, respectively, compared with devices based on flat ITO electrodes. The enhanced performance is related to the anti-reflection and light-scattering properties of ITO nanorods, which enhance incident light intensity and light-trapping property.

Introduction

Solar cells based on polymeric materials are being extensively used for electrical energy production because of their low production cost, large-area production, and low weight. Massive research on solution-processed polymer bulk heterojunction (BHJ) solar cell devices has led to dramatic enhancement in performance in the past decade.[1] However, the power conversion efficiency (PCE) of polymer BHJ solar cells is still somewhat lower than that of their inorganic counterparts. Therefore, the PCE must be further improved to promote polymer BHJ solar cells in practical applications. One of the key issues involved in increasing device performance is the enhancement of optical absorption of the photoactive layer. However, because polymer solar cells (PSCs) have a multilayer structure consisting of layers with different complex refractive indexes, the absorption of light at each layer and the reflection at interfaces of the layers prevent more light from entering the photoactive layer, thus resulting in a low photocurrent.[2] Moreover, because of the low charge carrier mobility of polymer semiconductors, a thick photoactive layer leads to high carrier recombination losses and a large series resistance that deteriorate device performance. Therefore, the thickness of the photoactive layer is typically less than 150 nm, which is less than its intrinsic absorption length; thus, the incident light cannot be completely absorbed.[3] Methods of enhancing the light absorption capability of a photoactive layer without compromising PCE are, therefore, of great interest to academia and industry.

Innovative PSC structures have attracted great attention because their light-trapping characteristic efficiently enhances light absorption.[4] Nanoimprint lithography,[5-7] laser interference lithography,[8,9] and mechanical rubbing[10] have been used to create nanostructures on hole-transporting and photoactive layers of PSCs, and notable improvements in PCE have been reported. In addition to the texturing of organic layers, incorporating inorganic nanostructures,

such as zinc oxide and ITO nanorods, on electrodes is also of great benefit to PSCs because of the anti-reflective[11,12] and light trapping[13,14] characteristics of the nanostructures. Further, ITO nanorods lead to significant improvement in PCE.[15-18] Because ITOs cannot be easily nanostructured by etching,[19] ITO nanorods are conventionally fabricated using molecular beam epitaxy,[11] oblique angle deposition,[15-18,20,21] plasma etching,[22] catalyst-mediated vapor–liquid–solid method,[23] or radio frequency magnetron sputtering deposition.[24] However, because these fabrication procedures are expensive, the fundamental understanding and development of ITO-nanorods-based PSCs and other optoelectronic devices were hampered. Moreover, the height of ITO nanorods cannot be precisely controlled in most of these methods. Therefore, a relatively easy ITO nanorods fabrication procedure that can be used in the production of different optoelectronic devices must be developed.

In this study, we show that an ITO film on a commercially available ITO-coated glass substrate can be etched into ITO nanorods through wet-chemical etching within a few minutes. The ITO nanorods are selectively formed in regions exposed to phosphoric acid by covering the remaining area of the ITO electrodes with an Al protective layer. The transmittance and the light-scattering capability are shown to be enhanced. Because the ITO nanorods enhance incident light intensity and trapped light in the photoactive layer, the short-circuit current density (J_{SC}) and the PCE of the ITO-nanorods-based PSCs were improved by 67% and 46%, respectively.

Experimental

Polymer solar cell devices were fabricated on patterned and cleaned ITO glass substrates (Uni-Onward Corp., 0.7 mm thick, 7 ohm/sq). An Al protective layer was deposited outside the active areas of the surface of the ITO substrates using a shadow mask at a deposition rate of 0.2

Å/s. The substrate was then submerged in phosphoric acid at 40 °C for 10 min to form ITO nanorods in the areas not covered by Al. For Devices B and C, the ITO nanorods were cleaned with acetone, isopropanol, deionized water, and UV-ozone before spin coating PEDOT–PSS as a hole-transporting layer. Thereafter, poly(3,4-ethylenedioxythiophene)–poly(styrenesulfonate) (PEDOT–PSS, Clevios P VP AI 4083) was blended with isopropanol and Triton X-100 in 50:50:1 volume ratio for better wetting property. The PEDOT‐PSS blend was spin coated at speeds of 2500 rpm, 500 rpm, and 6000 rpm for Devices A, B, and C, respectively. The substrates were annealed at 120 °C for 20 min to remove moisture. A dichlorobenzene blend solution of poly(3-hexylthiophene) (P3HT, Rieke Metals, Inc.) and [6,6]-phenyl-C61-butyric acid methyl ester (PCBM, Solenne BV) was prepared in a ratio of 1:1 by weight (P3HT:PCBM = 20 mg/ml:20 mg/ml), and the blend was then coated and annealed at 120 ℃ for 10 min to form the photoactive layer. Finally, the solar cell devices were obtained by depositing 40 nm Ca and 70 nm Al as cathode. The deposition rates of Ca and Al were 0.2 Å/s and 1 Å/s, respectively. All the devices were 4 mm^2 in area.

A Keithley 2400 source measure unit was used for device characterization, and the current density-voltage curves were plotted. Photocurrent measurements were performed under simulated air mass 1.5 global irradiation at an intensity of 100 mW/cm^2 using a xenon lamp-based solar simulator (Oriel 96000, 150 W). A field emission scanning electron microscope (FESEM, JEOL JSM-7600F) was used for scanning electron microscope (SEM) measurements. Dark-field microscopy images were recorded using an optical microscope with an Epiplan 50×/0.7 HD objective (E990, Carl Zeiss). The transmittance and absorbance were measured with a microspectrometer (SD1200-LS-HA, StreamOptics Co.).

Results and discussion

The experimental procedure for the fabrication of ITO nanorods is shown in Figure 1a. The photographic images of the patterned ITO-coated glass substrate were recorded after each fabrication step (Figures 1b–d). The central region of a single substrate (Figure 1b) was patterned for four devices (the schematic diagram of the devices on the single substrate is shown in Figure S1). A protective layer of Al was selectively deposited through a metal mask outside the central region of the pre-patterned ITO surface (Figure 1c); thus, the ITO nanorods are formed only inside the central region (see Supplementary Information for more details regarding sample preparation). The ITO nanorods were formed gradually inside the central region after the substrate was submerged in phosphoric acid maintained at 40 °C. The regions containing the ITO nanorods are more transparent than the ITO film (Figures 1b and d). Moreover, a dramatic color difference can be observed in the photographic images taken with a white reflective light as background (see insets in Figures 1b, 1d, and S2). To understand the ITO nanorods formation mechanism, the SEM images of the substrates were recorded at different etching times (Figures 1e–j). The thickness of the ITO film on the substrate is ~250 nm (Figure 1e). Deep cracks can be seen in the early stage of etching, and the cracks grow as the etching time increases (Figures 1f and g). The primary structural feature of the substrate etched for 10 min is a nanorod layer with a continuous ITO layer below. The ITO nanorods are vertically oriented with diameters ranging from approximately 30 nm to 105 nm and heights of ~250 nm, which is equal to the thickness of the ITO film. However, a very long etching time results in an over-etched ITO nanorod layer with regions lacking ITO above the glass substrate and ITO nanorods with nonuniform heights (Figures 1h–j). The electrical properties of the 2-mm long ITO nanorod film inside the central region were measured with a multimeter. The resistance of the bare ITO film was ~10 ohm. For

an etching time of 10 min, the resistance of the ITO nanorod layer increased to ~50 ohm. A further increase in etching time leads to a significant increase in resistance to a few hundred ohms. The energy-dispersive X-ray spectroscopy analysis indicates that the stoichiometries of the ITO nanorods and the ITO film are similar (Figure S4). Although the investigation of the ITO nanorods formation mechanism is outside the scope of the current research, we suppose that the oxidation-reduction reactions in the Al, ITO, and phosphoric acid system lead to the formation of ITO nanorods, because the ITO nanorods were not formed when there was no Al protective layer on the substrate (Figure S3).

Further experiments are required to understand the ITO nanorods formation mechanism.

The optical properties of the ITO nanorods were investigated using transmittance spectroscopy and dark-field microscopy. The bare ITO film exhibits transmittance peaks at 480 nm and 710 nm owing to Fabry–Pérot resonance (Figure 2a).[25] The transmittance of the etched substrates varies slightly with etching time for wavelengths below 500 nm. However, a remarkable enhancement in transmittance can be observed in a wavelength range of 500 nm to 1000 nm. For wavelengths below 800 nm, maximum transmittance was achieved in 10 min. Therefore, the formation of ITO nanorods results in increase of transmittance, which is an essential characteristic of an anti-reflective coating.[26] The effective medium theory considering a layer comprising two mediums with indices n_1 and n_2 and volume fractions f_1 and f_2 has been used to investigate the anti-reflective characteristics of nanostructures, and reduced reflection and enhanced transmission were reported.[27] Moreover, the dark-field microscopy image of the ITO nanorods with 10 min etching time (Figure 2d) is brighter than that of the bare ITO film (Figure 2b). Because dark-field microscopy includes only scattered light, the brighter image of the ITO nanorods proves the light-scattering nature of the ITO nanorods. These optical

characteristics of the ITO nanorods such as high transmittance and the light-scattering nature enhance the performance of PSCs. Because of the adequate nanorod morphology, the excellent light transmittance, and the light-scattering property, the etching time for ITO nanorods formation was selected to be 10 min during the fabrication of PSCs.

Previous studies attributed the improved performance of the ITO-nanorods-based PSCs to the reduced charge carrier transport distance, increased charge collection efficiency, and differences in transmission spectra.[15-18] Because the ITO nanorods protrude into the photoactive layer, which primarily contributes to the enhanced PCE, they cannot be easily identified. Therefore, three device architectures were fabricated in this study for comparison (Figure 3a). Devices B and C contain ITO nanorods and are compared with Device A having a planar ITO film (left panel of Figure 3a). The gaps between the ITO nanorods in Device B are filled with PEDOT–PSS, which is a hole-transporting material, (middle panel of Figure 3a) whereas the PEDOT–PSS coating is uniformly covered on the ITO nanorods in Device C (right panel of Figure 3a). The PEDOT–PSS was blended with isopropanol and Triton X-100 for improving wetting on the ITO nanorods. The filling of the gaps between the ITO nanorods (Figure 3c) and the coverage of the ITO nanorods surface (Figure 3e) by the blend solution can be controlled by adjusting the spin-coating speed between 500 rpm to 6000 rpm. When the spin-coating rate is 2500 rpm, the PEDOT–PSS blend is partly filled in the gaps and partly on the surface of the ITO nanorods (Figure 3d). Spin coating of such a blend solution on a planar ITO film also results in a good wetting property (Figure 3b). No remarkable protrusions can be found on the flat PEDOT–PSS surfaces (Figures 3b and c). The influence of the PEDOT–PSS coating on the optical properties of the ITO nanorods was then investigated. As the spin-coating speed of the PEDOT–PSS is reduced, the transmittance decreases (Figure 3f); hence, the brightness of the dark-field

microscopy image decreases (Figures 2d–f). The dark-field microscopy image of the PEDOT–PSS coated ITO film is slightly brighter than that of the bare ITO film because the PEDOT–PSS coated ITO film exhibits a higher transmittance in the wavelength range of 540 nm to 700 nm (Figures 2b and c).

A blend of P3HT and PCBM was used for depositing the photoactive layer. The blend solution was deposited not only on the substrates with flat PEDOT–PSS surfaces but also on the PEDOT–PSS coated (conformal) ITO nanorods (Figure S5). Good polymer infiltration is achieved, and no air gaps can be observed (Figures 3f and S6). Therefore, the structures of Devices A, B, and C shown in Figure 3a can be realized. The thickness of the photoactive layer can be easily controlled by varying the spin-coating speed, and it can be determined by estimating the distance between the top of the PEDOT–PSS layer and the cathode (Devices A and B) or the distance between the crest of the PEDOT–PSS covered ITO nanorod and the cathode (Device C). It should be noted that the amount of photoactive material in Device C is underestimated because it is also present in the valleys between the PEDOT–PSS coated (conformal) ITO nanorods.

The characteristics of Devices A, B, and C with different photoactive layer thicknesses were investigated and compared (Figures 4 and S7 and Table 1). The photovoltaic parameters of the devices are summarized in Table 1, and the two representative *J*-*V* curves of Devices A, B, and C with similar thicknesses (~140 nm and ~180 nm) are shown in Figure 4a. The maximum averaged values of J_{SC} and PCE of Device A with thickness of 220 nm are 6.34 mA/cm^2 and 2.10%, respectively (Table 1 and Figure S7a). These results are consistent with the theoretical calculations of [28] that reported an oscillating behavior with two maxima at 80 nm and 220 nm, considering optical reflection and interference within a multilayer device. The oscillatory nature

of J_{SC} and PCE is related to the oscillatory behavior of the number of photons absorbed in the active layer.[28] For Device B, both J_{SC} and PCE decrease as the thickness of the photoactive layer decreases from 180 nm to 130 nm (Table 1 and Figure S7b). Because Device B contains ITO nanorods with light-scattering characteristics, the model considering optical interference within a multilayer device may not be suitable for Device B. We suppose that, at a constant voltage, the lower J_{SC} value and lower PCE of Device B with a thicker photoactive layer may be attributed to a smaller electric field, which results in an increase in recombination rate and a reduction in exciton dissociation rate. The fill factor (FF) also suffers from such drawbacks and is the lowest for the thickest Devices A and B (Table 1). Nevertheless, most of the FFs of Device B are also less than 50% whereas most of those of Device A are greater than 50%. Further, the performance of Device B is better than that of Device A when both the Devices have similar photoactive layer thickness (Figure 4a). The average values of J_{SC} and PCE of Device B with a 180 nm photoactive layer are 9.70 mA/cm^2 and 2.61%, respectively, which is an improvement of 67% and 35%, respectively, when compared with Device A. The J_{SC} and PCE of Device B with a 140 nm photoactive layer are also enhanced by 59% and 46%, respectively, when compared with Device A. The superior performance of Device B is attributed to the increased light absorption (Figure 4b) resulting from the enhanced transmittance and light-scattering characteristics of the ITO nanorods. Moreover, the light-trapping effect inside the photoactive layer may be further strengthened because the light reflected from the cathode can cause scattered reflection from the nanorods.[19] Regarding Device C, as the photoactive layer thickness decreases, the J_{SC} and PCE first decrease and then increase (Table 1 and Figure S7c). Similar to those of Device B, most of the FFs of Device C are less than 50% except for the one corresponding to the thinnest photoactive layer. The J_{SC} and PCE of Device C with a 150 nm photoactive layer are enhanced

by 44% and 17%, respectively, when compared with Device A (Figure 4a and Table 1). These superior characteristics can also be attributed to the increased transmittance and the light-scattering characteristics of the ITO nanorods. However, the performance of Device C is inferior to that of Device B, even through Device C appears to gain more benefits, such as better charge collection and reduced charge transport distance, from its device structure.[15,16,18] The poorer performance of Device C is attributed to the lower open-circuit voltage (V_{OC}) and shunt resistance (R_{SH}) than those of Device B. The V_{OC} and R_{SH} of Device C are approximately 0.57 V and 10^4–10^6 ohm cm^2, respectively, whereas those of Device B (and Device A) are approximately 0.62 V and ~10^6 ohm cm^2, respectively. In addition, R_{SH} is determined from the *J*–*V* characteristics measured under dark conditions.[29] The smaller value of V_{OC} can be attributed to the incomplete coverage of PEDOT–PSS on the surface of the ITO nanorods. In the absence of the PEDOT–PSS coating between the anode and the photoactive layer, a non-ohmic contact that may decrease V_{OC} is formed.[30] The smaller value of R_{SH} is due to the electrode proximity effects[15,18] and the nonuniform current distribution around the nanorods.[15] In summary, for devices with similar thicknesses, though the FFs of Devices B and C are lower than that of Device A and the V_{OC} of Device C is lower than those of Devices A and B, the PCEs of Device B and Cs can be easily improved by a larger value of J_{SC} thus resulting in higher PCEs than that of Device A. Because the performance of Device B is superior to that of Device C, the enhanced incident light intensity and the light-trapping characteristic are believed to be the most important advantages of ITO nanorods.

Conclusion

In this study, we successfully developed a wet etching method for fabricating ITO nanorods with similar height within a few minutes. The desirable optical characteristics of PSCs such as

high transmittance and extensive light-scattering ability were observed with ITO nanorods. Moreover, the incorporation of ITO nanorods in the PSCs resulted in superior J_{SC} and PCE compared with those of the device with a planar ITO film. By comparing devices with different structures, the enhanced incident light intensity and light-trapping characteristic are shown to be the major causes of performance improvement. The benefits of ITO nanorods are not limited to the contents in this paper, and ITO nanorods fabricated using a simple, fast, and reproducible fabrication method may advance applications such as light-emitting diodes and solar cells.

Acknowledgements

This work was supported by the National Science Council of Taiwan under grant number NSC100-2112-M-033-008-MY3.

Notes and references

1. G. Li, R. Zhu and Y. Yang, *Nature Photon.*, 2012, **6**, 153–161.

2. G. Dennler, M. C. Scharber and C. J. Brabec, *Adv. Mater.*, 2009, **21**, 1323–1338.

3. H. A. Atwater and A. Polman, *Nat. Mater.*, 2010, **9**, 205–213.

4. T. G. Deepak, G. S. Anjusree, Sara Thomas, T. A. Arun, Shantikumar V. Nair and A. Sreekumaran Nair, *RSC Adv.*, 2014, **4**, 17615.

5. S. I. Na, S. S. Kim, S. S. Kwon, J. Jo, J. Kim, T. Lee and D. Y. Kim, *Appl. Phys. Lett.*, 2007, **91**, 173509.

6. J. B. Emah, R. J. Curry and S. R. P. Silva, *Appl. Phys. Lett.*, 2008, **93**, 103301.

7. D. H. Ko, J. R. Tumbleston, L. Zhang, S. Williams, J. M. DeSimone, R. Lopez and E. T. Samulski, *Nano Lett.*, 2009, **9**, 2742–2746.

8. L. Müller-Meskamp, Y. H. Kim, T. Roch, S. Hofmann, R. Scholz, S. Eckardt, K. Leo and A. F. Lasagni, *Adv. Mater.*, 2012, **24**, 906–910.

9. K. S. Nalwa, J. M. Park, K. M. Ho and S. Chaudhary, *Adv. Mater.*, 2011, **23**, 112–116.

10. K. Li, H. Zhen, Z. Huang, G. Li and X. Liu, *ACS Appl. Mater. Interfaces*, 2012, **4**, 4393–4397.

11. C. O'Dwyer, M. Szachowicz,, G. Visimberga, V. Lavayen, S. B. Newcomb and C. M. S. Torres, *Nat. Nanotechnol.*, 2009, **4**, 239–244.

12. D. J. Seo, J. P. Shim, S. B. Choi, T. H. Seo, E. K. Suh and D. S. Lee, *Opt Express.*, 2012, **20**, A991–A996.

13. A. Raman, Z. Yu and S. Fan, *Optics Express*, 2011, **19**, 19015–19026.

14. A. P. Vasudev, J. A. Schuller and M. L. Brongersma, *Optics Express*, 2012, **20**, A385–A394.

15. P. Yu, C. H. Chang, M. S. Su, M. H. Hsu and K. H. Wei, *Appl. Phys. Lett.*, 2010, **96**, 153307.

16. D. A. Rider, R. T. Tucker, B. J. Worfolk, K. M. Krause, A. Lalany, M. J. Brett, J. M. Buriak and K. D. Harris, *Nanotechnology*, 2011, **22**, 085706.

17. M. H. Hsu, P. Yu, J. H. Huang, C. H. Chang, C. W. Wu, Y. C. Cheng and C. W. Chu, *Appl. Phys. Lett.*, 2011, **98**, 073308.

18. M. K. Fung, Y. C. Sun, A. Ng, A. M. Ng, A. B. Djurisić, H. T. Chan and W. K. Chan, *ACS Appl. Mater. Interfaces*, 2011, **3**, 522–527.

19. Y. C. Chao, C. Y. Chen, C. A. Lin and J. H. He, *Energy Environ. Sci.*, 2011, **4**, 3436–3441.

20. A. L. Beaudry, R. T. Tucker, J. M. LaForge, M. T. Taschuk and M. J. Brett, *Nanotechnology*, 2012, **23**, 105608.

21. C. H. Chang, P. Yu and C. S. Yang, *Appl. Phys. Lett.*, 2009, **94**, 051114.

22. J. G. V. Dijken and M. J. Brett, *J. Vac. Sci. Technol. A*, 2012, **30**, 040606.

23. Q. Wan, E. N. Dattoli, W. Y. Fung, W. Guo, Y. Chen, X. Pan and W. Lu, *Nano Lett.* 2006, **6**, 2909–2915.

24. J. H. Park, H. K. Park, J. Jeong, W. Kim, B. K. Min and Y. R. Do, *J. Electrochem. Soc.* 2011, **158**, K131–K135.

25. C. H. Chiu, P. Yu, C. H. Chang, C. S. Yang, M. H. Hsu, H. C. Kuo and M. A. Tsai, *Opt. Express*, 2009, **17**, 21250–21256.

26. S. Chattopadhyay, Y. F. Huang, Y. J. Jen, A. Ganguly, K. H. Chen and L. C. Chen, *Mat. Sci. Eng. R*, 2010, **69**, 1–35.

27. H. K. Raut, V. A. Ganesh, A. S. Nair and S. Ramakrishna, *Energy Environ. Sci.*, 2011, **4**, 3779–3804.

28. Y. M. Nam, J. Huh and W. H. Jo, *Sol. Energy Mater. Sol. Cells*, 2010, **94**, 1118–1124.

29. G. Li, V. Shrotriya, J. Huang, Y. Yao, T. Moriarty, K. Emery and Y. Yang, *Nature Mater.*, 2005, **4**, 864–868.

30. L. Yang, T. Zhang, H. Zhou, S. C. Price, B. J. Wiley and W. You, *ACS Appl. Mater. Interfaces*, 2011, **3**, 4075–4084.

Table 1 Photovoltaic parameters of polymer solar cells with planar and nanostructured ITO electrodes, measured under 100 mW cm^{-2} AM 1.5G illumination. Performance metrics reported are the average of at least 3 devices. Numbers in parentheses are for the best performing cells.

Device type	Thickness [nm]	J_{SC} [mA/cm^2]	V_{OC} [V]	FF [%]	PCE [%]
A	260	5.82	0.609	51	1.83
		(5.97)	(0.611)	(54)	(1.94)
	220	6.34	0.616	54	2.10
		(6.64)	(0.620)	(56)	(2.16)
	210	5.79	0.613	57	2.01
		(5.93)	(0.615)	(57)	(2.07)
	190	5.80	0.611	54	1.93
		(5.91)	(0.614)	(56)	(2.04)
	140	4.20	0.601	54	1.35
		(4.61)	(0.607)	(56)	(1.49)
B	180	9.70	0.617	44	2.61
		(10.19)	(0.625)	(46)	(2.88)
	170	8.68	0.621	49	2.62
		(8.81)	(0.626)	(52)	(2.80)
	160	8.17	0.618	45	2.25
		(8.53)	(0.627)	(48)	(2.45)
	140	6.69	0.615	48	1.97
		(6.91)	(0.618)	(49)	(2.07)
	130	6.11	0.626	53	2.05
		(6.43)	(0.636)	(56)	(2.30)
C	160	8.24	0.573	47	2.20
		(8.56)	(0.581)	(49)	(2.24)
	150	6.05	0.540	49	1.59
		(6.30)	(0.548)	(53)	(1.61)
	120	6.41	0.572	44	1.61
		(6.77)	(0.581)	(50)	(1.94)
	110	6.31	0.565	46	1.64
		(6.61)	(0.573)	(47)	(1.74)
	100	6.34	0.581	53	1.93
		(6.51)	(0.595)	(55)	(2.06)

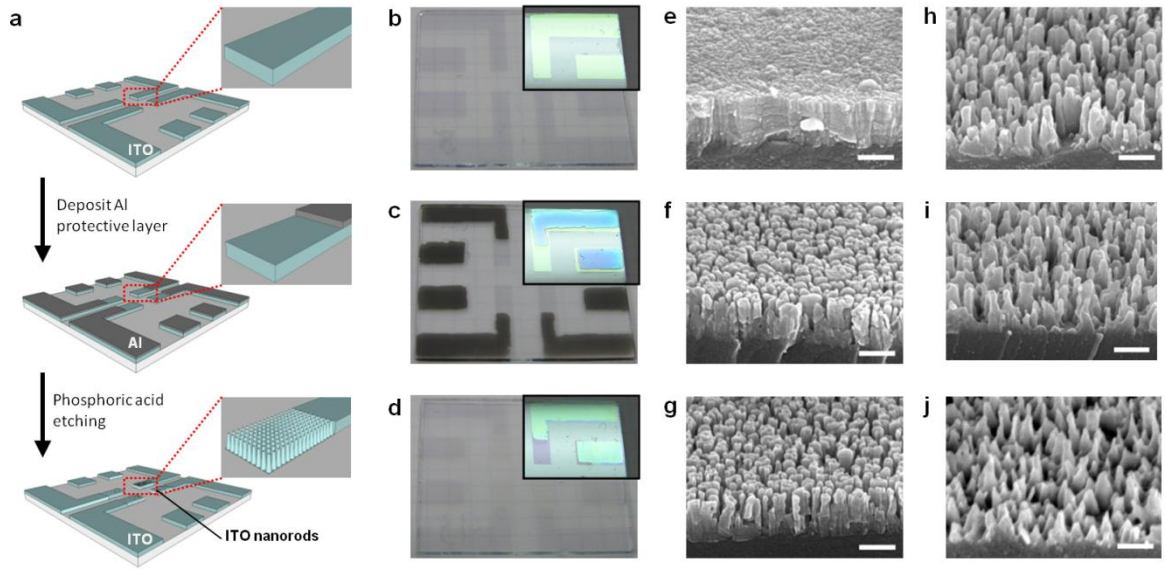

Fig. 1 Images of each fabrication step. (a) Schematic illustration of the fabrication procedures to produce ITO nanorods. Photographic images of the ITO-coated glass substrate (b) before Al protective layer deposition, (c) after Al protective layer deposition and (d) after 10 min phosphoric acid etching. The insets show the images with a white reflective light as background. SEM images of the ITO layers etched for (e) 0 min, (f) 8 min, (g) 10 min, (h) 32 min, (i) 60 min, and (j) 90 min. The scale bar corresponds to 200 nm.

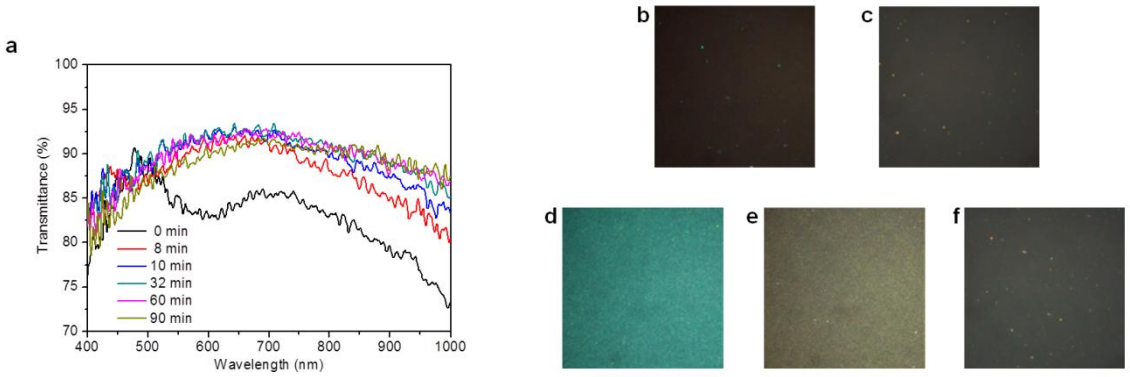

Fig. 2 Optical properties of the ITO nanorods. (a) Transmittance spectrum of the ITO etched for various times. Dark-field microscope images of (b) the ITO film, (c) the ITO film coated with PEDOT:PSS at 2500 rpm, (d) the ITO nanorods, (e) the ITO nanorods coated with PEDOT:PSS at 6000 rpm, and (f) the ITO nanorods coated with PEDOT:PSS at 500 rpm.

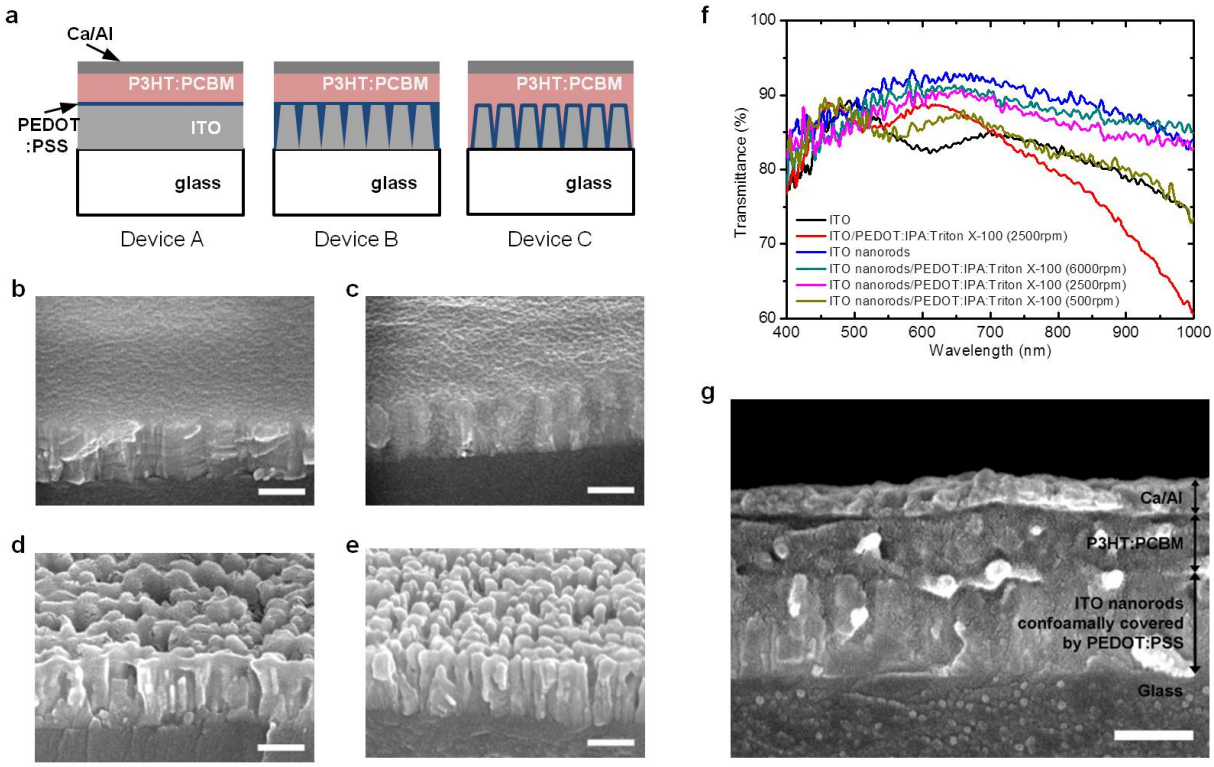

Fig. 3 Device structures and characteristics. (a) Schematic illustration of structures of device A, B, and C. SEM images of (b) the ITO film coated with PEDOT:PSS at 2500 rpm, (c) the ITO nanorods coated with PEDOT:PSS at 500 rpm, (d) the ITO nanorods coated with PEDOT:PSS at 2500 rpm, and (e) the ITO nanorods coated with PEDOT:PSS at 6000 rpm. (f) Transmittance spectrum of various substrates. (g) SEM cross-sectional image of Device C with ~160 nm photoactive layer above the crest of PEDOT:PSS covered ITO nanorod. The scale bar corresponds to 200 nm.

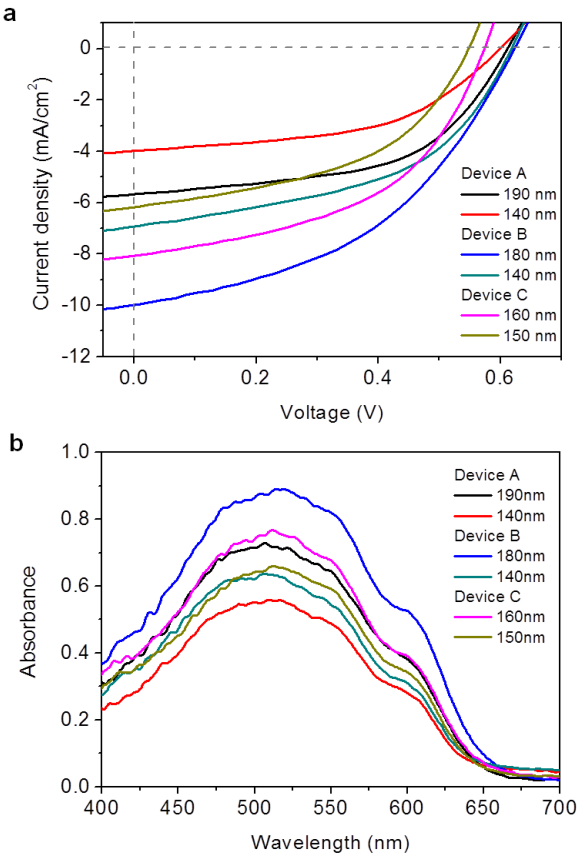

Fig. 4 The performance of devices with various structures and thicknesses. (a) Current density-voltage characteristics of device A, B, and C. (b) The absorbance of the photoactive layers with various thicknesses.